buildings

MDPI

Article

Seismic Behavior of Concrete Beam-Column Joints Reinforced with Steel-Jacketed Grouting

Xinzhuo Yang [1], Yiding Dong [2], Xi Liu [2,*], Tong Qiu [1] and Jian Zhou [1]

[1] Northwest Engineering Corporation Limited, Xi'an 710065, China; yangxinzhuo123@126.com (X.Y.); qiutong8546@126.com (T.Q.); jianzhounec@163.com (J.Z.)
[2] School of Civil Engineering, Chang'an University, Xi'an 710064, China; 2021028005@chd.edu.cn
* Correspondence: xliu1205@126.com

Abstract: Joints in frame structures often fail before beams and columns in an earthquake and are a key part of reinforcement. In this study, to enhance the seismic performance of concrete frame structures, a steel-jacketed grouting composite reinforcement method is proposed by combining reinforcement technology, steel cladding technology, and eco-efficient materials from grouting technology. This method effectively utilizes the advantages of various materials, avoids major demolition and construction, and reduces waste and resource consumption. In order to verify the feasibility and effectiveness of the reinforcement method, one of the original joint specimens with a scale of 1:3 and one of the reinforced joint specimens were designed and tested. The experiments involved reversed cyclic testing of beam–column to measure its seismic behavior. The seismic performance indexes such as failure characteristics, hysteretic properties, and the energy dissipation capacity of the specimens were analyzed, and the corresponding finite element model was established. The influence of key parameters such as reinforcement range, steel plate thickness, and grout strength on its seismic performance was explored. The research shows that the method can effectively improve the seismic performance of the joints, and seismic performance indexes such as bearing capacity, ductility, and energy consumption of the specimens are significantly improved. The test results of the established finite element model are in good agreement. The variable parameter analysis of the finite element shows that the thickness of the steel plate has little influence on its bearing capacity. With the increase in the reinforcement range of the clad steel and the strength of the grouting material, the bearing capacity of the specimen increases. The research results can provide a reference for the reinforcement of frame structure joints.

Keywords: steel jacketed; grouting; beam-column joints; seismic performance; finite element method

Citation: Yang, X.; Dong, Y.; Liu, X.; Qiu, T.; Zhou, J. Seismic Behavior of Concrete Beam-Column Joints Reinforced with Steel-Jacketed Grouting. *Buildings* **2024**, *14*, 3239. https://doi.org/10.3390/buildings14103239

Academic Editors: Harry Far and Hugo Rodrigues

Received: 17 September 2024
Revised: 9 October 2024
Accepted: 9 October 2024
Published: 12 October 2024

1. Introduction

Joints are one of the important structural components of reinforced concrete frame structures, which play the role of internal force transfer between beam and column members. Brittle shear failure of joints will make the force transfer mechanism of the original frame structure system fail and will lead to serious damage or collapse of the structure in strong earthquakes. Many seismic disasters show that a large number of existing frame structures in China still have hidden dangers of insufficient shear-bearing capacity in the core area of beam-column joints, which seriously affects the safety performance of structures [1–5]. Therefore, it is necessary to improve the shear capacity of the beam-column joints in existing buildings by appropriate seismic strengthening methods, so as to prevent buildings whose seismic performance does not meet requirements from collapsing in strong earthquakes.

In order to reduce the risk of earthquake disasters in existing buildings, scholars at home and abroad have carried out a lot of research on the seismic strengthening of beam-column joints, and put forward various strengthening methods for reinforced concrete beam-column joints. At present, seismic strengthening techniques for beam-column joints

in RC structures include increasing sections [6,7], a steel hoop [8,9], FRP wrapping [10–12], composite strengthening [13,14], etc. These strengthening methods can effectively improve the shear-bearing capacity of beam-column joints and improve their ductility. Engindeniz et al. [15] summarized the representative joint repair and reinforcement technologies and analyzed the engineering application, labor cost, applicability, and reinforcement effect of various methods. Its internal mechanism is mainly the transfer of a plastic hinge at the beam end [16]. There are also methods for strengthening the overall structure—such as adding BRB supports [17]—to improve the seismic performance of the structure.

To cope with different scenarios, scholars have proposed new reinforcement methods different from the traditional ones. For example, Oleg R. [18] investigated the behavior of the joints of steel-fiber-reinforced concrete (SFRC) and reinforced concrete beams under load at various loading stages. Shan Z.W. [19] introduced a novel direct fastening steel jacket that can increase both flexural strength and stiffness. This novel strengthening method features straightforward installation and swift strengthening as direct fastening is used to connect steel plates together to form a steel-jacketed column. This new connection method can quickly and stably connect two steel components together by driving high-strength fasteners into them. Tsonos A.D. [20] proved high-strength steel-fiber-reinforced concrete (HSFC) and ultra-high-strength steel-fiber-reinforced concrete (UHSFC) jackets, which are more effective than other strengthening schemes in improving the hysteresis performance of existing substandard reinforced concrete (RC) structural members. Hung C.C. et al. [21] proposed a method for repairing external beam-column joints with ultra-high-performance concrete (UHPC) sheathing reinforced with high-strength steel mesh. The results show that the UHPC sheath reinforced with high-strength steel mesh shows excellent ability to reduce extensive joint diagonal cracks and column splitting cracks, which not only restores the seismic performance of the damaged beam-column joints but also significantly improves their seismic performance. At present, the method is only the material innovation or partial form innovation of the original reinforcement method, and there are few methods combining reinforcement from various methods.

In view of the excessive increase in the load on the upper part of the column, the single increase in the section will affect the use of space, and the method of a Baotou steel grouting reinforcement joint is proposed to solve such problems. The combined Baotou steel grouting and reinforcement technology can effectively solve such problems in the reconstruction project. Thus, this study adopts the coupling technology of clad steel and grouting to strengthen the side joints of concrete frame, and designs and tests two 1:3 horizontal reciprocating tests of the side joints of the frame, including one unreinforced specimen and one reinforced specimen. The failure characteristics and seismic performance of the two specimens are compared and analyzed, the validity of the finite element model is verified, and then the key parameters of reinforcement (reinforcement range, steel plate thickness, grout strength, etc.) are analyzed using the finite element model.

2. Experimental Programs

2.1. Specimen Design

The prototype is derived from a typical multi-layer frame structure with a height of 3 m and a span of 5 m. Two RC frame joint specimens with a scale of 1:3 were produced, including one unreinforced specimen A-C and one reinforced specimen A-R-C. The concrete beams and columns are made of C40 concrete, with a column height of 830 mm and a column cross-section size of 200 × 200 mm^2. HRB400 rebar with a diameter of 10 mm is used for the bearing longitudinal reinforcement, HRB400 rebar with a diameter of 6 mm is used for the stirrup. The space between the stirrups is 50 mm, and the space between the stirrups in the unsealed area in the middle of the column is 100 mm. The steel plate adopts Q335B steel plate and the welding rod adopts E50. The strength of grout is not less than C50. The reinforcement ratio is 1.57% (8C10), the stirrup ratios are 1.508/0.754% and 1.14/0.57% (C6@50/100), the beam length is 1330 mm, the cross-section size of the beam is 150 × 300 mm^2, and the reinforcement ratio of the lower part is 0.935% (3C10). The stirrup

ratio is 1.492/0.746% (A6@50/100). The specific parameters and reinforcement structure are shown in Figure 1.

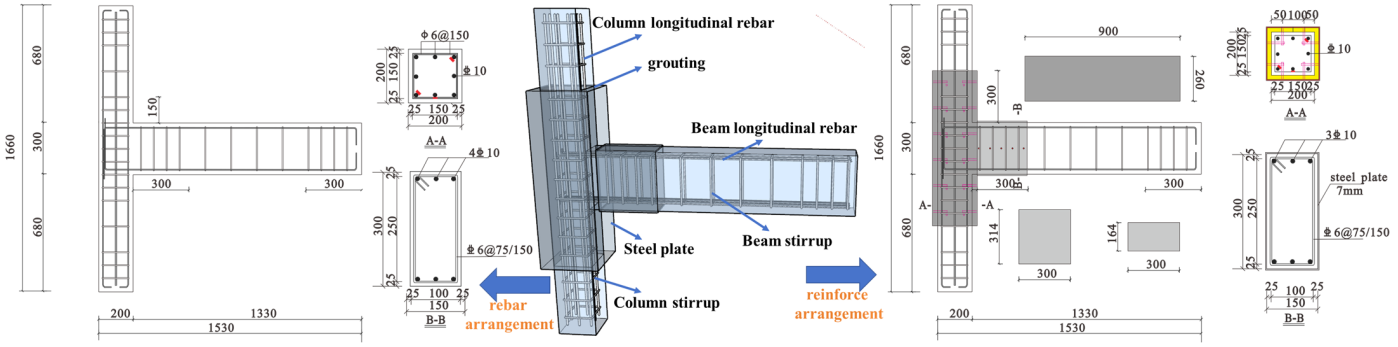

Figure 1. Dimensions and reinforcement details of specimens (mm).

2.2. Strengthening RC Frame Joint Construction Process

Polish the rust off the surface of the steel bar and prepare the area for attaching the strain gauge. Once attached, wrap the strain gauge with gauze and epoxy resin, and secure it to the steel bar cage. Clean any excess debris from the reinforcement mold according to design specifications before pouring. After forming the specimen, plant reinforcement on it and reserve holes for the steel plates. Pass the steel plates through these holes and fix them in place, welding any gaps between plates and securing with high-strength grouting material. Once these steps are completed, allow the specimen to cure for 28 days. The process of strengthening joints with steel plates is shown in Figure 2.

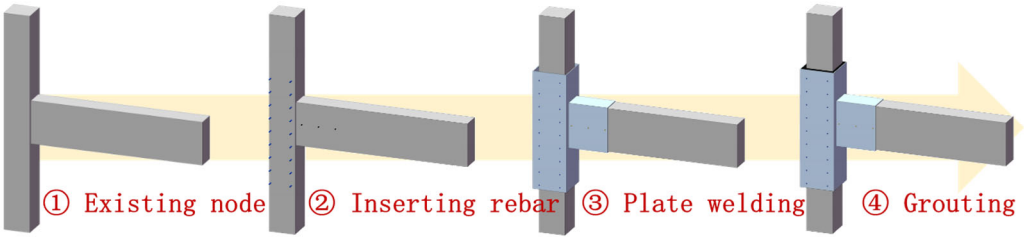

Figure 2. Strengthening joint procedure with steel sheet.

2.3. The Loading System

Considering the *p*-Δ effect, which cannot be ignored under large axial pressure, the joint is loaded at the column end. The axial load is applied by the reaction beam and hydraulic jack, and the horizontal repeated thrust is applied by the electro-hydraulic servo actuator (MTS). The test loading device is shown in Figure 3. In this test, the method of low-cycle loading is used to measure the seismic performance of the reinforced joint. At the initial stage of loading, the column top axial load is first applied to the predetermined axial pressure ratio by the hydraulic jack to ensure the free extension of the beam end in the vertical deformation process and to ensure that the joint does not produce initial internal force. Then, the electro-hydraulic servo actuator applies low cyclic horizontal load to the column top. The horizontal cyclic load is controlled by displacement, marked by the cracking of the specimen. According to American ANSI/AISC341-10 regulations [22], horizontal loading adopts an interlayer displacement angle control loading scheme, and the loading system is shown in Figure 4. Each stage is cycled three times to observe the loading process and test the phenomenon of the specimen in detail. When the bearing capacity of the specimen decreases to 85% of the maximum bearing capacity or when the loading reaches 1/35 of the displacement angle, the test is stopped.

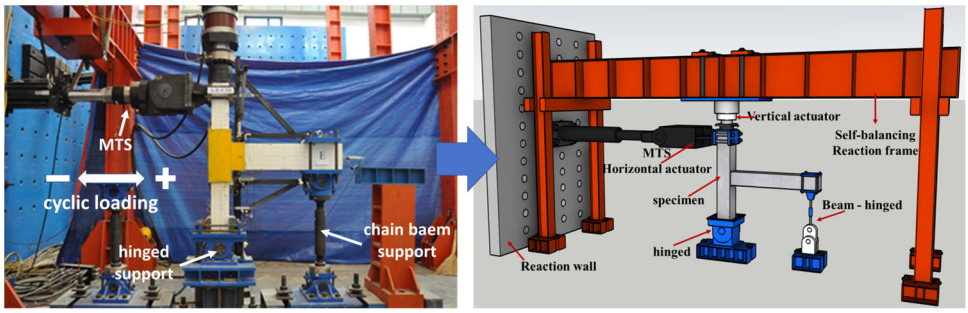

Figure 3. Test setup.

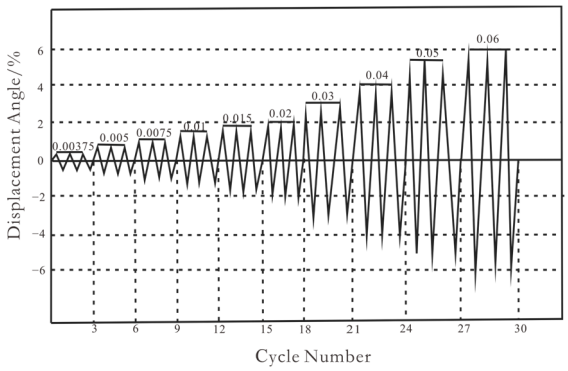

Figure 4. Loading history.

3. Failure Process and Experimental Results

3.1. Failure Process

The joints were pre-loaded before the formal loading. At the pre-loading stage, no cracks were detected at either joint. After the pre-loading is complete, a drift of 0.2% is applied to the joint. Due to the absence of a steel jacket, numerous small cracks have been observed at the beam end of the A-C joint, while no cracks are found at this stage.

Upon the application of the secondary displacement load (with a displacement rate of 0.35%), a through crack appears at the A-C joint beam end, with a small crack width. At this point, the A-R-H joint begins to show only minor cracks. As the load increased further, the width and number of cracks increased on the beams of each joint. When the sixth level of loading (with 1% drift) was reached, a large crack began to appear at the beam end of the A-C joint, and the number of major cracks in the A-R-H joints also increased significantly. In the late loading period, the number of diagonal cracks in the two joints continued to increase as the loading continued.

At the eighth level of loading (2% drift), concrete spalling initiated at the beam-column junction of the A-C joints, and diagonal cracks started to develop at the beam ends of the A-R-H joints. This phenomenon escalated with the continued application of load. During the third cycle of the 14th level load (with a drift rate of 3.5%), the bearing capacity of both joints decreased to 85% of the ultimate load. The sound of the reinforcement being pulled apart was clearly heard during loading. At the end of the test, the specimens were dissected and it was found that the reinforcement in the A-C joint had broken (as shown in Figure 5). On the contrary, the A-R-H joints, due to the presence of the steel jacket, showed that although the concrete near the steel jacket started to spall off at the ninth level of loading (with a drift rate of 2.75%), this phenomenon gradually increased with the increase in loading. Eventually, when the load reaches the third cycle of level 11 (drift rate of 4.25%), the bearing capacity of the A-R-H joints also decreases to 85% of the ultimate load, again accompanied by the sound of the steel pulling apart, indicating damage to the joints.

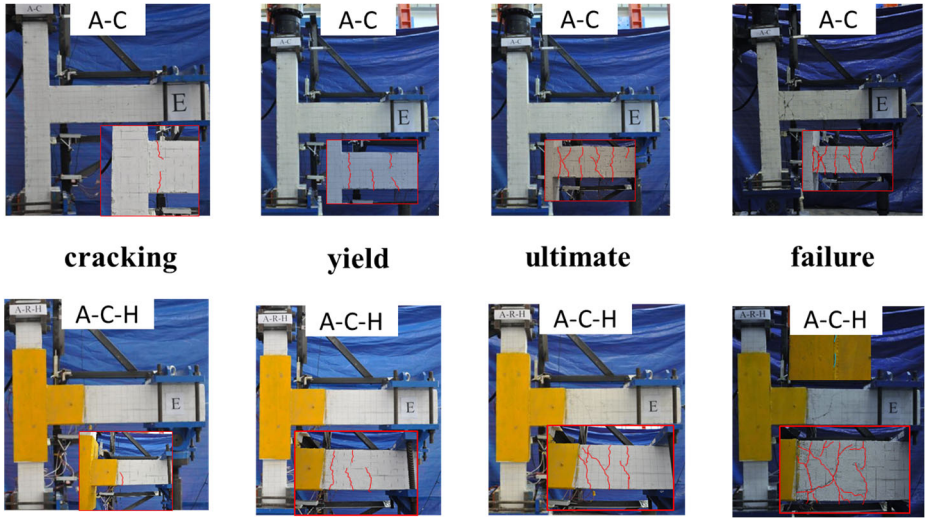

Figure 5. Typical damage patterns in each stage.

It can be seen from the experiments that the use of steel plates increased the bearing capacity of the joints. From the beginning to the end of loading, the failure process of the two joints was basically the same, going through the elastic deformation stage, crack formation stage, yielding stage, and final failure stage. For the specimen of A-C, the damage was mainly concentrated at the beam-column interconnecting piece, with a maximum crack width of 2 mm and concrete spalling. In contrast, the damage in specimens A-R-H was located far from the beam-column junction. Figure 6 illustrates that the concrete damage near the bottom of the beam was primarily focused in close proximity to the steel sleeve. This suggests that the presence of a steel sleeve at the connection point between the beam and column effectively restricts the development of a plastic hinge at the end of the beam. Overall, both joints exhibited the "beam hinge mechanism" damage pattern expected by the design.

Figure 6. Final failure mode.

3.2. Hysteretic Performance

As shown in Figure 7, the hysteresis curves of the two joints showed a similar overall trend, with both joints passing through the elastic, yield, ultimate, and failure stages. In the elastic phase, the hysteresis curves of the two specimens are close to a straight line and change linearly. When the specimen entered the yield stage, the area of the hysteresis loop gradually increased, and the hysteresis loop of A-R-H was fuller than that of A-C, indicating that the hysteresis response of the A-R-H joints was better than that of the A-C joints. In addition, the ultimate load capacity of the A-R-H joint exceeds that of the A-C joint, indicating that it has a stronger hysteresis dissipation capability.

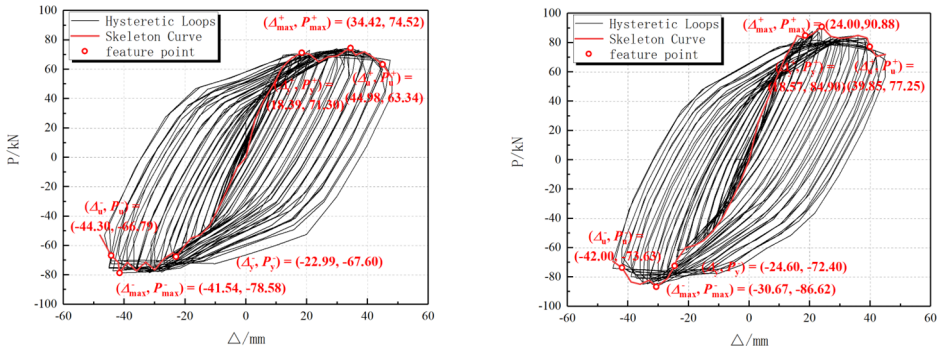

Figure 7. Hysteretic performance: (**a**) the hysteresis curve of A-C; (**b**) the hysteresis curve of A-R-H.

The steel sleeve in the A-R-H joint is located at the beam-column junction and plays a key role in the overall stressing process of the joint. During the elastic stage, the A-R-H joint exhibits significantly higher stiffness compared to the A-C joint. As it enters the yielding stage, the steel sleeve becomes involved in dissipating energy, resulting in a more complete hysteresis loop for the A-R-H joint. This increase in energy dissipation greatly enhances the bearing capacity of the A-R-H joint, surpassing that of the A-C joint by 10%.

3.3. Energy Dissipation Capacity

In this study, the equivalent viscous damping coefficient h_e, h_e was used as an indicator of energy dissipation capacity. The larger the value, the higher the energy dissipation capability of the component. Figure 8 shows the calculation results of h_e, and its corresponding formula is shown in Equation (1).

$$h_e = \frac{1}{2\pi} \cdot \frac{S_{ABC} + S_{CDA}}{S_{\triangle OBF} + S_{\triangle ODE}} \tag{1}$$

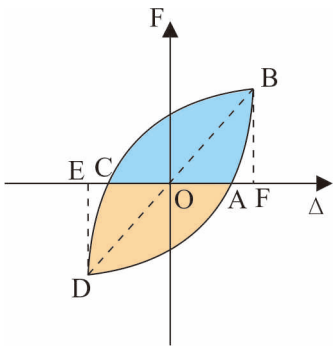

Figure 8. Equivalent viscosity coefficient calculation.

The viscous damping coefficient was determined by analyzing the area enclosed by each hysteresis loop, and the comparative outcomes for the two samples are presented in

Figure 9. From Figure 9, it can be seen that the equivalent viscous damping coefficients of the two joints changed little until the 18th cyclic loading (with a drift rate of 1%), and the difference was not significant. This is because the two specimens are still in the elastic phase and have comparable energy dissipation capacity. From the 19th hysteresis (drift rate of 1.5%) to the 30th hysteresis (drift rate of 3.5%), the equivalent viscous damping coefficients increased significantly as the specimens entered into the yielding stage, with a stepwise increase. In addition, the equivalent viscous damping coefficient of A-R-H joints is significantly higher than that of A-C joints, indicating that the energy dissipation capacity of A-R-H joints is better than that of A-C joints after entering the yield stage.

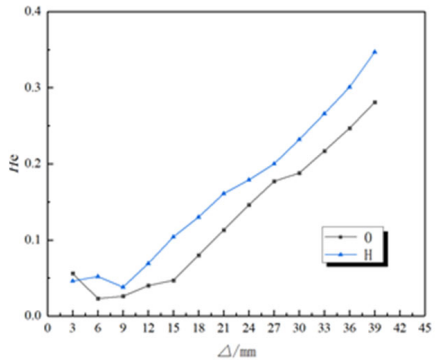

Figure 9. Equivalent viscous damping coefficient.

The A-C joint reached its maximum value at the 48th cycle of loading (3% drift) and then failed and stopped loading. In contrast, the equivalent viscous damping coefficient of the A-R-H joint peaked at the 42nd cycle of loading (2.5% drift). Even at the final stage of failure, the equivalent viscous damping coefficient of A-R-H was still higher than that of A-C. In conclusion, the energy dissipation capacity of beam-column joints can be significantly improved by introducing steel plates at the joints.

3.4. Stiffness Degradation

Stiffness is a measure of a structure's ability to withstand elastic deformation when subjected to external forces in structural engineering. When the specimen is repeatedly loaded at low circumferences, its stiffness decreases. This means that as the displacement amplitude increases, less load is needed to achieve the same displacement value. The decrease in stiffness can be used to indicate the cumulative level of damage to the structure under repeated loads. In this study, the stiffness of the specimen is expressed as positive stiffness K_i, and its calculation formula is shown in Equation (2) [23]. The stiffness degradation curves are shown in Figure 10.

$$K_i = \frac{|+F_i| + |-F_i|}{|+\Delta_i| + |-\Delta_i|} \tag{2}$$

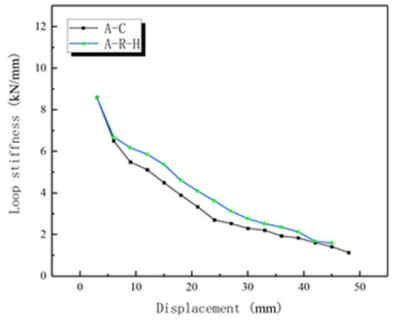

Figure 10. Stiffness degradation curve.

Within the figure, the trends of the two joints are basically the same. Initially, the initial stiffnesses of specimens A-C and A-R-H are comparable, which is due to the fact that both of them are in the state of elastic deformation during the initial loading stage. Both A-C and A-R-H experienced rapid stiffness degradation over the loading displacement range of 6 mm (drift rate of 0.35%) to 30 mm (drift rate of 1.8%). The rate of stiffness decay slows down after entering the yielding stage. From Figure 10, it can be seen that the stiffness of A-R-H is always higher than that of A-C, both in the initial stiffness and in the subsequent loading stages, which suggests that the provision of steel plates at the beam-column joints can help to enhance the stiffness of the joints.

3.5. Deformation Capacity

Ductility is an important index to measure the deformation capacity of a structure, and a key parameter to evaluate the seismic performance of a structure under low circumferential repeated loads. The ductility coefficient (μ) is generally used to express the ratio of ultimate displacement (D_u) to yield displacement (D_y). Various methods, such as the farthest point method, geometric drawing method, and equal energy method [23], can be employed to determine the yield displacement. In this study, the isoenergetic method illustrated in Figure 11 was utilized for determining the yield displacement. Table 1 presents the results of the displacement ductility coefficients for the two joints. Table 1 clearly shows that the deformation capacity of A-R-H is better than that of A-C. The ultimate displacement of A-R-H is about 42 mm, while that of A-C is 48 mm. Additionally, the A-R-H joint exhibits higher forward and reverse displacement ductility coefficients compared to A-C. These findings suggest that the steel sleeve plays a positive role in improving the overall ductility performance of the joint.

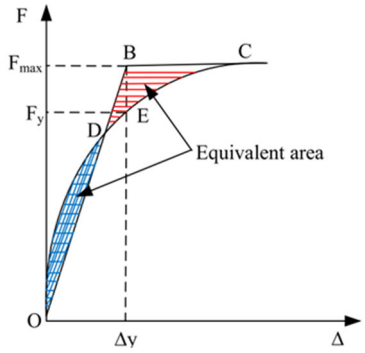

Figure 11. Calculation diagram of equal energy method.

Table 1. Ductility coefficient of joints.

Specimen	Load Direction	Yield Displacement Dy/mm	Ultimate Displacement Du/mm	Ductility Factor Du/Dy	Average Value
A-C	Forward	18.39	44.98	1.76	2.07
	Negative	−22.99	−44.30	2.37	
A-R-H	Forward	18.57	39.85	3.05	2.43
	Negative	−24.60	−42.00	1.80	

4. The Key Parameters of Strengthening Beam-Column Joints

4.1. Establishment of Finite Element Model

4.1.1. Element Selection

In this study, the finite element model of the A-R-H joint is established using ABAQUS software (version 2016). Among them, the original concrete columns, steel plates, and grout use solid units—three-dimensional eight-node reduced integral solid elements (C3D8R). The steel bars were simulated using truss elements, two-dimensional three-node (T3D2).

4.1.2. Material Constitutive Model

In this study, the reinforcement constitutive simulation developed by Fang Zihu of Shenzhen University was employed [24]. The subroutine of the reinforcement hysteresis model written by the Professor can simulate the degradation of structural strength and stiffness caused by the bond-slip between reinforcement and concrete under cyclic load. Figure 12 shows the reinforcement hysteresis model.

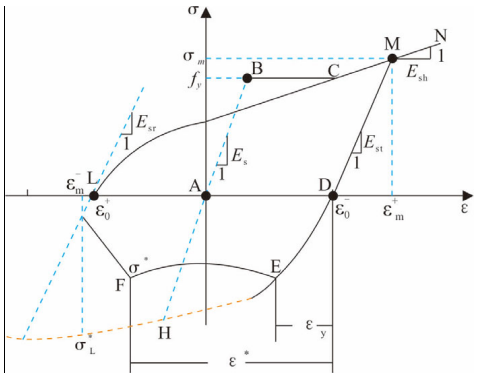

Figure 12. Fang Zihu's reinforcement hysteresis model.

The ABAQUS software offers three constitutive models of concrete materials: the Concrete Smeared cracking model, the Concrete Brittle cracking model, and the Concrete Damage Plasticity (CDP) model. This investigation selects the CDP model as the concrete model for simulation, which accounts for the damage accumulation during the loading process of concrete and is suitable for the simulation of monotonic, cyclic, and dynamic loads under low confining pressures. Considering the stress state of the concrete in the steel-encased region, the reinforced area concrete's constitutive model utilizes the uniaxial compressive stress–strain relationship curve suggested by Mander et al. [25]. The Mander model is formulated to address the effective lateral confinement effect of reinforcement on concrete, which is particularly applicable to the enhanced constraint zone in columns. The uniaxial compressive constitutive relationships for concrete under different constraint conditions used in this investigation are displayed in the Figure 13.

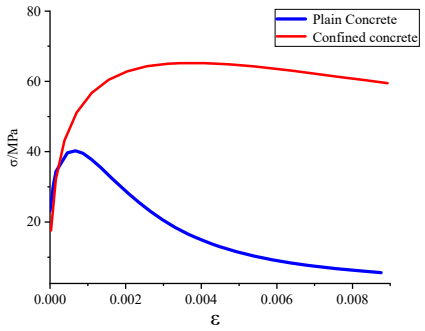

Figure 13. The constitutive relationships of concrete and confined concrete under compression.

The tensile constitutive model for concrete is adopted from the GB50010-2010 [26], which provides the uniaxial tensile stress–strain relationship curve for concrete. The calculation of the constitutive relationship is shown in Figure 14.

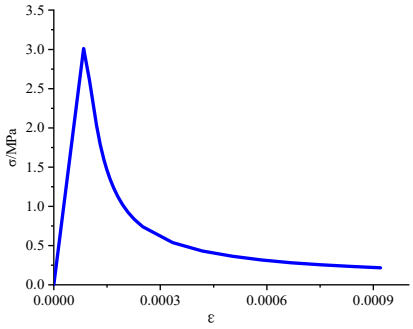

Figure 14. Constitutive relationship of concrete under tension.

4.1.3. Definition of Contact

When defining the contact between surfaces, it is important to consider both tangential and normal behaviors. This is because there are tangential friction and normal extrusion pressures present in both old and new concrete. In ABAQUS software, the "penalty" friction function is used to implement tangential behavior. The model sets the friction coefficient between the original concrete and post-cast grout at 0.6, while representing normal behavior with hard contact.

An embedded approach is required to simulate the bond-slip relationship between reinforcement and concrete. Interfaces between old and new concrete, as well as between the steel plate and concrete, were modeled using surface-to-surface contact with normal hard contact and tangential Coulomb friction. The friction coefficient for the interface between old and new concrete was set to 0.8, while the friction coefficient for the interface between the steel plate and concrete was set to 0.6 [27]. Under the premise of ensuring accuracy, after several grid divisions, the seed density of the concrete parts is finally selected to 50, that is, the size of the grid is 50 mm × 50 mm × 50 mm. The grid size of the reinforced steel plate and structural adhesive is 50 mm × 50 mm × 50 mm, and the steel bar adopts the truss unit and the grid is divided into 50 mm. The grid of each component is shown in Figure 15 below. The model underwent structured mesh generation, with a seed density of 20 applied to the concrete components, and the meshing illustration for each component is shown in the following Figure 15. The model has four reference points (RPS), as shown in Figure 16. Among them, RP-Top and RP-PUSH are the coupling points of the column top and column end, respectively, which are used to apply axial pressure and lateral displacement. RP-BOTTOM and RP-BRAM are the coupling points of the column bottom and beam end, respectively, and 6 degrees of freedom constraints are applied to them. The lateral displacement is applied at the coupling point RP-PUSH at the end of the column, and the cyclic loading regime is the same as that of the test.

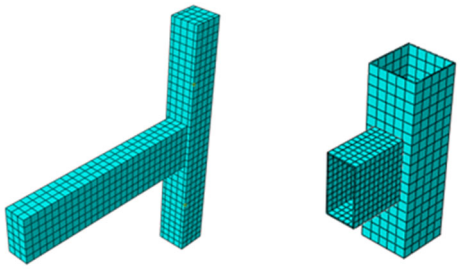

Figure 15. Mesh generation.

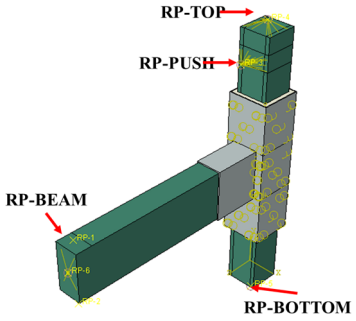

Figure 16. Finite element model.

4.2. Finite Element Results Analysis

Figures 17 and 18 show the comparison between the simulation results and the test results of the reinforced joints. It can be seen from the figures that the skeleton curves obtained by the finite element analysis are in good agreement with the test results, especially in the post-elastic stage. There are some differences between the experimental structure and the simulation results because the experimental boundary conditions are slightly different from the experimental boundary conditions. The simulated stiffness and the experimental stiffness in the elastic stage show a slight variance, which is commonly observed in other studies. This difference can be attributed to the idealized boundary conditions used in simulations compared to real-world conditions as well as potential defects in the loading device. By using this model, we can gain insight into different design parameters, such as different ranges of clad steel reinforcement, different thicknesses of steel plate, and different strengths of grout.

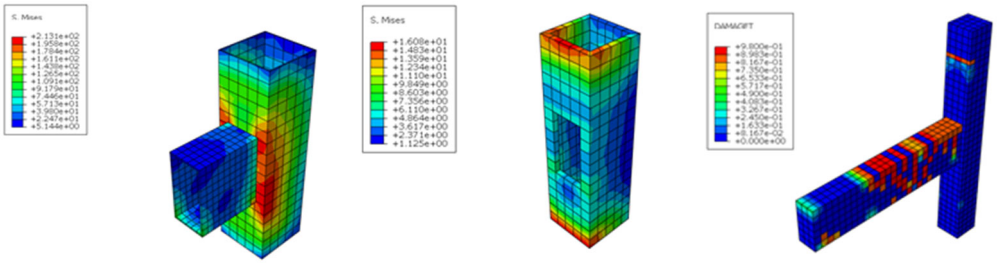

Figure 17. A-R-H nephogram: (**a**) steel; (**b**) grouting; (**c**) concrete.

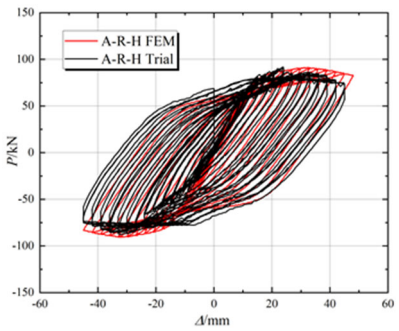

Figure 18. Comparison of experimental and simulated values A-R-H.

4.3. Parametric Study

On the basis of the verified finite element method, a parametric analysis of the joints is carried out. By changing different parameter variables, different joint simulation components are established, and the mechanical characteristics of the joints are studied under different thicknesses of steel plate, different reinforcement ranges of steel envelope, and

different strengths of grout. The analysis results are shown in Figures 19 and 20. By comparing the hysteresis curves of each simulation component, the following conclusions can be drawn:

1. The hysteretic curves of each model member show a jumping phenomenon in the first few cycles, indicating that the concrete has good resistance to deformation at this stage. In the later stage, with the increase in the number of vertical load cycles, the maximum load value in the hysteretic curve decreases, indicating that the concrete is damaged at this stage;
2. The hysteretic curve of the reinforced member shows a sharp spindle shape, indicating that the model member itself has good seismic performance, and the deformation in the later stage under the load controlled by repeated vertical displacement is relatively large, indicating that the concrete has been damaged to a certain extent, and the deformation and bearing capacity has decreased at this stage. The hysteretic curves of the member models strengthened by the adhesive steel show a smooth spindle shape, and the deformation of the hysteretic curves in the later stage is small, which indicates that the seismic performance of the members strengthened by the adhesive steel is improved;
3. The area of hysteretic curves of the model members reinforced with steel is larger than that before reinforcement, which indicates that the model members reinforced with steel plates have better energy dissipation capacity and plastic deformation resistance, indicating that the bearing capacity of the reinforced members is improved and the stiffness decline is alleviated. The shape of the three hysteresis curves is very similar, all of them are smooth shuttle shapes, but the difference between them is that the area of the hysteresis curves increases with the increase in the thickness of the steel plate used in the model, the strength of the grout, and the reinforcement range. The area of the hysteresis curve increases with the increase in grout strength.

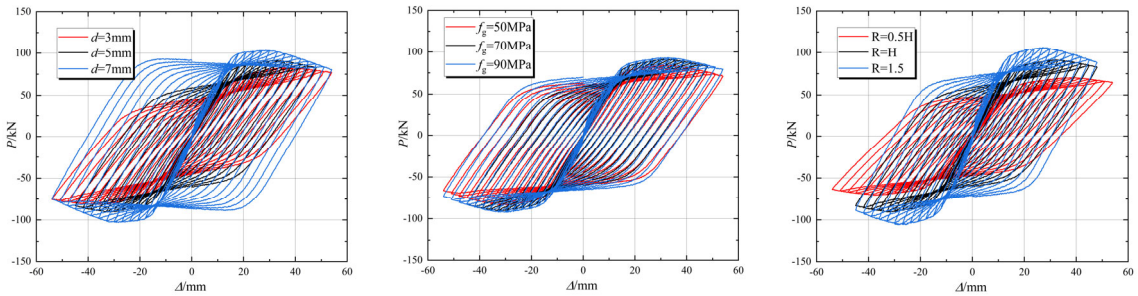

(**a**) (**b**) (**c**)

Figure 19. Hysteresis curve of finite element joint: (**a**) thickness of steel plate; (**b**) strength of grout material; (**c**) reinforcement range.

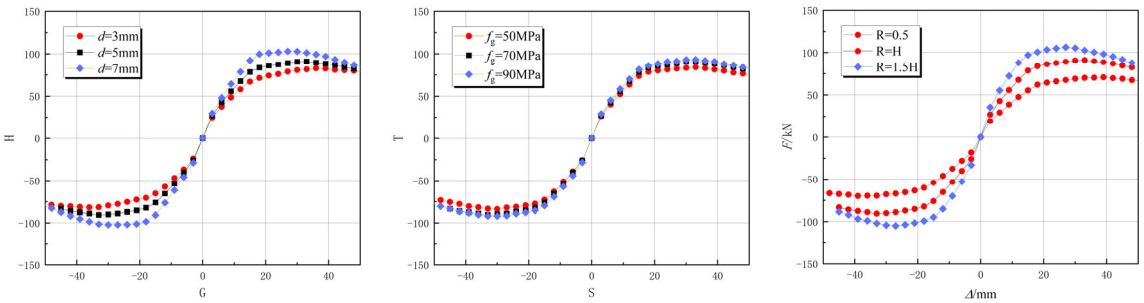

(**a**) (**b**) (**c**)

Figure 20. Skeleton curve of finite element: (**a**) thickness of steel plate; (**b**) strength of grout material; (**c**) reinforcement range.

By comparing the skeleton curves of each simulated component, the following conclusions can be drawn:

During the initial loading stage, the curves overlap. The steel plate does not have an impact on the initial loading stage, and the load is supported by concrete and steel bars. The reinforced specimens show significantly higher yield load, peak load, and ultimate displacement compared to the comparison specimens, indicating that the reinforcement of steel plates effectively enhances the bearing capacity and deformation capacity of the specimens. When comparing skeleton curves of joint members reinforced with different thicknesses of steel plates, it is evident that specimens with 7 mm thick steel plates exhibit better bearing capacity and displacement ductility than those with 5 mm and 3 mm thick steel plates. The overall trend in the development of both skeleton curves is similar. As negative loading members enter failure stages, there is a dramatic decrease in bearing capacity with increasing displacement due to bonded steel plate failure. Additionally, it can be observed that grouting material strength has minimal effect on edge joint bearing capacity but has a greater impact on middle joints. With increased reinforcement range, joint member bearing capacity increases primarily due to the enhanced role of the steel plate as the reinforcement range expands.

As depicted in Figure 21, the cumulative energy consumption of joints with strong reinforcement consistently exceeds that of weakly reinforced joints from the onset of loading until failure. However, due to limited displacement ductility, energy consumption is depleted earlier and ceases. A comparison of the cumulative energy consumption of differently reinforced joints reveals similar energy dissipation capacities in the initial loading stage, while specimens with higher reinforcement strength exhibit a gradual increase in cumulative energy dissipation during late-stage loading, resulting in greater overall energy dissipation compared to those with lower reinforcement strength. The thickness and range of steel plate reinforcement significantly impact its energy dissipation capacity and are positively correlated. Grout strength has minimal influence on the component's energy dissipation capacity.

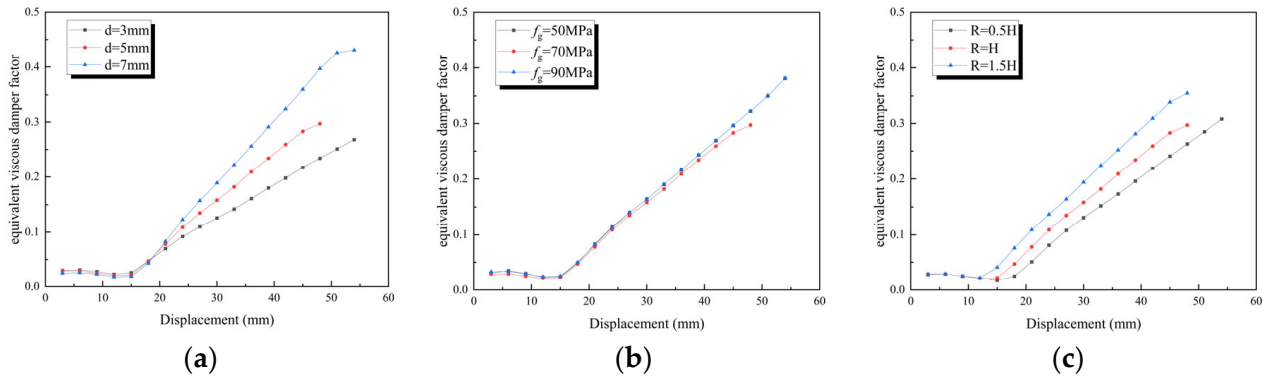

Figure 21. Equivalent viscous damping coefficient: (**a**) thickness of steel plate; (**b**) strength of grout material; (**c**) reinforcement range.

As depicted in Figure 22, the initial stiffness of the reinforced joint is notably lower than that of the joint specimen prior to reinforcement. As the loading displacement increases, the reinforced joint experiences rapid degradation in stiffness, while the unreinforced joint degrades at a slower pace. The figure illustrates that there is a positive correlation between the reinforcement range and steel plate thickness with the initial stiffness of the component. Additionally, it shows that the reinforcement range has the most significant impact on stiffness degradation, followed by the steel plate thickness, while grout strength has minimal influence. This indicates that adjusting the initial stiffness of the member can be achieved through design modifications to the steel plate thickness and reinforcement range.

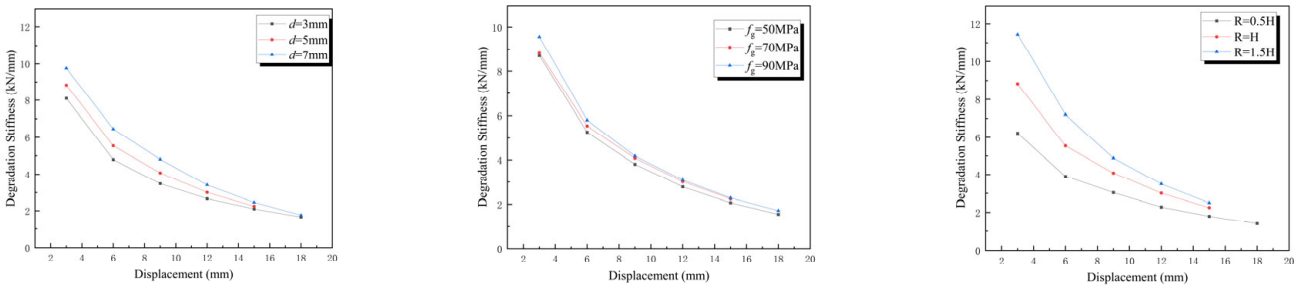

(**a**) (**b**) (**c**)

Figure 22. Stiffness degradation curve: (**a**) thickness of steel plate; (**b**) strength of grout material; (**c**) reinforcement range.

5. Conclusions

In this work, a method for strengthening concrete frame joints with steel-jacketed grouting coupling is proposed, and its seismic performance is studied experimentally. Based on the verified finite element model, the effects of reinforcement range, steel plate thickness, and grout strength on the seismic performance of the joint are studied and parameterized. The experiment and the FEA results support the following:

1. The seismic performance of the joints is improved significantly by using Baotou steel grouting. The feasibility and effectiveness of the reinforced technology are verified by experiments. The hysteretic curve of the reinforced specimen is more obvious in the cracking stage but the pinching phenomenon is gradually improved in the late loading stage, and the initial stiffness and ductility are improved. It shows that this technology can effectively improve the seismic performance of the joint;
2. By comparing with the test results, the joint refinement model established in this paper can well-reflect the failure state and hysteretic performance of the components in the actual test. Considering the reinforcement range, steel plate thickness, and grout strength conditions, the finite element parameter extension analysis models of the frame edge joint are established.
3. Analysis of the finite element simulation results shows that with the increase in the steel bonding range, the stress resistance ability of the steel skeleton joints is gradually improved, which can improve the deformation resistance and load-bearing ability of the whole bearing member. The area of hysteresis curve increases with the increase in grouting strength and reinforcement range. The steel plate thickness has little effect on the seismic performance of the joint members, and the overall bearing capacity increases with the increase in steel plate thickness. The joint bearing capacity increases with the increase in grouting material strength and reinforcement range. The thickness of the steel plate and the range of reinforcement should be considered when this method is used to strengthen joints.

Author Contributions: X.Y.: Data curation, Formal analysis. Y.D.: Investigation, Software, original draft. X.L.: Conceptualization, Methodology, Validation. T.Q.: Project administration, Supervision. J.Z.: Funding acquisition, Visualization. All authors have read and agreed to the published version of the manuscript.

Funding: The Natural Science Foundation of Shaanxi Province (Grant No. 2020JQ-388); Shaanxi Provincial Department of Education Youth Innovation Team Project (21JP008); Shaanxi Province key research and development plan project (2023-YBSF-249); Fund Project of the Science and Technology Department of Shaanxi Province (2024SF-YBXM-609); Fund Project of the Science and Technology Department of Shaanxi Province (2024GX-YBXM-177); Fund Project of the Power Construction Corporation of China (XBY-KJ-2022-04).

Data Availability Statement: The original contributions presented in the study are included in the article, further inquiries can be directed to the corresponding author.

Conflicts of Interest: Author Xinzhuo Yang was employed by the company Northwest Engineering Corporation Limited. The remaining authors declare that the research was conducted in the absence of any commercial or financial relationships that could be construed as potential conflicts of interest.

References

1. Wang, X.; Wan, P.C.; Zhu, Z.Y.; Wang, K.; Cao, D.; Yang, Y.; Yang, D.; Zhang, L. Research on seismic performance of new prestressed precast beam-column sleeve concrete frame joints. *Structures* **2024**, *61*, 105954. [CrossRef]
2. Li, G.; Fan, Y.; Du, N. Performance Study of Concrete Beam-Column Joints in Building Steel Structures Under High-Intensity Vibration. *Int. J. Multiphysics* **2022**, *16*, 107–118.
3. Obaidat, Y.T. Cyclic behavior of interior RC beam-column joints strengthened with NSM-CFRP ropes. *Structures* **2022**, *37*, 735–744. [CrossRef]
4. Zhang, Y.; Ding, K.W. Study on seismic behavior of fabricated beam-column bolted joint. *Struct. Eng. Mech.* **2022**, *82*, 801–812.
5. Gao, X.L.; Lin, C. Prediction model of the failure mode of beam-column joints using machine learning methods. *Eng. Fail. Anal.* **2021**, *120*, 105072. [CrossRef]
6. Bindhu, K.R.; Mohana, N.; Sivakumar, S. New Reinforcement Detailing for Concrete Jacketing of Nonductile Exterior Beam-Column Joints. *J. Perform. Constr. Facil.* **2016**, *30*, 04014192. [CrossRef]
7. Gholampour, A.; Hassanli, R.; Mills, J.E. Experimental investigation of the performance of concrete columns strengthened with fiber reinforced concrete jacket. *Constr. Build. Mater.* **2019**, *194*, 51–61. [CrossRef]
8. Xue, J.Y.; Ren, G.Q.; Zhang, J.H.; Xu, D. Seismic performance of semi-tenon joints reinforced by steel angle in traditional timber buildings. *Adv. Struct. Eng.* **2020**, *23*, 2318–2332. [CrossRef]
9. Shoukry, M.E.; Tbarabia, A.M.; Abdelrahman, M.Z. Seismic retrofit of deficient exterior RC beam-column joints using steel plates and angles. *Alex. Eng. J.* **2022**, *61*, 3147–3164. [CrossRef]
10. Zia, A.; Pu, Z.; Holly, I.; Umar, T.; Tariq, M.A.U.R. Development of an Analytical Model for the FRP Retrofitted Deficient Interior Reinforced Concrete Beam-Column Joints. *Appl. Sci. Basel* **2022**, *12*, 2339. [CrossRef]
11. Hosseini, A.S.; Bahaari, M.R.; Lensani, M. Experimental and parametric studies of SCFs in FRP strengthened tubular T-joints under axially loaded brace. *Eng. Struct.* **2020**, *213*, 110548. [CrossRef]
12. Lin, J.P.; Wu, Y.F.; Smith, S.T. Width factor for externally bonded FRP-to-concrete joints. *Constr. Build. Mater.* **2017**, *155*, 818–829. [CrossRef]
13. Esmaeeli, E.; Danesh, F.; Tee, K.F.; Eshghi, S. A combination of GFRP sheets and steel cage for seismic strengthening of shear-deficient corner RC beam-column joints. *Compos. Struct.* **2017**, *159*, 206–219. [CrossRef]
14. Barmi, C.G.; Saghafi, M.H.; Golafshar, A. Providing a strategy to restore damaged RC beam-column joints with the combination of CFRP and HPFRCC. *Eng. Struct.* **2024**, *299*, 117148. [CrossRef]
15. Engindeniz, M.; Kahn, L.F.; Zureick, A.H. Repair and strengthening of reinforced concrete beam-column joints: State of the art. *ACI Struct. J.* **2005**, *102*, 187–197.
16. Behnam, B.; Lim, P.J.; Ronagh, H.R. Plastic Hinge Relocation in Reinforced Concrete Frames as a Method of Improving Post-earthquake Fire Resistance. *Structures* **2015**, *6*, 21–31. [CrossRef]
17. HHooshangi, M.A.; Hadianfard, A.J. The reliability assessment of the seismic demands of beams in chevron-braced frames and the factors affecting them. *Structures* **2024**, *66*, 106876. [CrossRef]
18. Ruano, G.; Isla, F.; Pedraza, R.I.; Sfer, D.; Luccioni, B. Shear retrofitting of reinforced concrete beams with steel fiber reinforced concrete. *Constr. Build. Mater.* **2014**, *54*, 646–658. [CrossRef]
19. Shan, Z.; Chen, L.; Liang, K.; Su, R.K.L.; Xu, Z. Strengthening Design of RC Columns with Direct Fastening Steel Jackets. *Appl. Sci. Basel* **2021**, *11*, 3649. [CrossRef]
20. Tsonos, A.D.; Kalogeropoulos, G. Analytical Model for the Design of HSFC and UHSFC Jackets with Various Steel Fiber Volume Fraction Ratios for the Retrofitting of RC Beam-Column Joints. *Sustainability* **2021**, *13*, 11209. [CrossRef]
21. Hung, C.-C.; Agrawal, S.; Hsiao, H.-J. Rehabilitation of seismically-damaged RC beam-column joints with UHPC and high-strength steel mesh reinforcement. *Eng. Struct.* **2024**, *305*, 117764. [CrossRef]
22. *ANSI/AISC 341-10*; Seismic Provisions for Structural Steel Buildings. American Institute of Steel Construction: Chicago, IL, USA, 2010.
23. Yu, J.; Xia, Y.; Guo, Z.; Guo, X. Experimental study on the structural behavior of exterior precast concrete beam-column joints with high-strength steel bars in field-cast RPC. *Eng. Struct.* **2023**, *299*, 117128. [CrossRef]
24. Fang, Z.H.; Zhen, Y.; Li, X.P. Steel hysteretic model of reinforced concrete structures. *Eng. J. Wuhan Univ.* **2018**, *51*, 613–619.
25. Mander, J.B.; Priestley, M.J.; Park, R. Theoretical stress-strain model for confined concrete. *J. Struct. Eng.* **1988**, *114*, 1804–1826. [CrossRef]
26. *GB 50010-2010*; Code for Design of Concrete Structures. China Architecture & Building Press: Beijing, China, 2011. (In Chinese)
27. Rabbat, B.; Russell, H. Friction coefficient of steel on concrete or grout. *J. Struct. Eng.* **1985**, *111*, 505–515. [CrossRef]